BRIEF PAPER

Range Points Migration Based Spectroscopic Imaging Algorithm for Wide-Beam Terahertz Subsurface Sensor

Takamaru MATSUI[†], ***Student Member and*** **Shouhei KIDERA**[†,††a)], ***Member***

SUMMARY Here, we present a novel spectroscopic imaging method based on the boundary-extraction scheme for wide-beam terahertz (THz) three-dimensional imaging. Optical-lens-focusing systems for THz subsurface imaging generally require the depth of the object from the surface to be input beforehand to achieve the desired azimuth resolution. This limitation can be alleviated by incorporating a wide-beam THz transmitter into the synthetic aperture to automatically change the focusing depth in the post-signal processing. The range point migration (RPM) method has been demonstrated to have significant advantages in terms of imaging accuracy over the synthetic-aperture method. Moreover, in the RPM scheme, spectroscopic information can be easily associated with each scattering center. Thus, we propose an RPM-based terahertz spectroscopic imaging method. The finite-difference time-domain-based numerical analysis shows that the proposed algorithm provides accurate target boundary imaging associated with each frequency-dependent characteristic.

key words: *terahertz imaging, subsurface imaging, range points migration, spectroscopic imaging, synthetic aperture processing, radar signal processing*

1. Introduction

One of the emerging technologies for scientific or engineering applications is terahertz (THz)-band imaging, which provides a distinct advantage over alternative imaging techniques in that it offers millimeter-order penetration depth and micrometer-order spatial resolution. Terahertz imaging sensors are employed in various applications, including nondestructive testing, chemical analysis, or medical diagnosis, owing to their characteristics that are advantageous. However, standard THz imaging systems (e.g., THz-TDS systems) generally require dielectric lenses to obtain high azimuth resolutions; this limits the penetration range that can be achieved while maintaining a certain azimuth resolution. In addition, the beam direction must be normal to the target surface to obtain sufficient reflection strength but if the depth of the object is unknown, the dielectric lens cannot be appropriately adjusted beforehand.

To address this issue, radar approaches, such as those based on the synthetic aperture (SA), have been considered to attain a depth-independent resolution [1], [2], inverse SA approach for moving target [3] and frequency-modulated continuous-wave (FMCW) radar [4], and its application to a personnel-scanning system [5], [6]. SA-based methods are advantageous when the distance between the covered surface and the sample is unknown and much longer than the focusing length; they provide a range-independent azimuth resolution. The synthetic-aperture-based (SA-based) methods usually incur high computational costs to provide a complete three-dimensional image, and their associated side- and grating-lobe effects generate unnecessary responses.

Recently, the range point migration (RPM) method has been proposed to solve the above mentioned issues of the SA-based method. This technique is particularly useful for short-range microwave radar [7], [8], and advanced subsurface imaging [9], [10]. In the RPM method, each location of the scattering centers is estimated using a group of measured ranges called range points via incoherent analysis, facilitating lower complexity imaging with high accuracy because of the suppression of undesirable responses usually caused by the coherent process. As a notable feature of the RPM, each scattering center is associated with the scattering phenomenon, such as the frequency-dependent effects of surface reflection.

Therefore, we propose an RPM-based spectroscopic imaging method, wherein the frequency-dependent response can be associated with time-frequency analysis in the preprocessing stage according to the basic scheme that we have recently proposed in [11]. The finite-difference time-domain (FDTD)-based numerical simulations, which is one of the most reliable forward solver, demonstrate that the proposed method can be used to accurately reconstruct the target boundary with accuracy within 10 μm, which cannot be achieved by the SA-based method.

2. Observation and Signal Model

Figure 1 illustrates the observation geometry. The surrounding media (e.g., plastic material), including a number of buried objects, is assumed to be homogeneous, low loss, and non-dispersive in the THz frequency band. A transmitter and a receiver are scanned or, alternatively, an array of multiple transmitters and receivers is located on the same plane. $s(\boldsymbol{L}, R)$ denotes the output of a range extraction filter (e.g., a matched filter) of each received signal as $s(\boldsymbol{L}, t)$, where $\boldsymbol{L} = (X, Y, 0)$ is the location of the transmitter and receiver (the same location in this model) and $R = \mathrm{c}t/2$ is defined using time, t. The propagation speed in air is c. The range points are determined by the local maxima of $s(\boldsymbol{L}, R)$, as presented in detail in [7], and divided into two

Manuscript received March 11, 2019.
Manuscript revised June 13, 2019.

[†]The authors are with Graduate School of Informatics and Engineering, University of Electro-Communications, Chofu-shi, 182–8585 Japan.
[††]The author is with JST, PRESTO, Kawaguchi-shi, 332–0012 Japan.
a) E-mail: kidera@ee.uec.ac.jp

DOI: 10.1587/transele.2019ECS6005

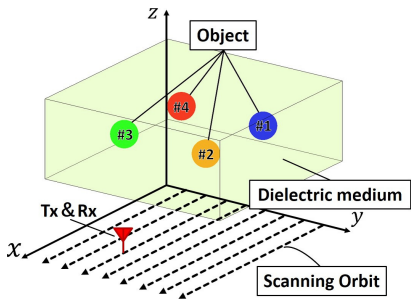

Fig. 1 Observation model.

groups: $\boldsymbol{q}_{1,i} = (\boldsymbol{L}_{1,i}, R_{1,i})$, where each point has a maximum at $s(\boldsymbol{L}, R)$ with respect to R, and $\boldsymbol{q}_{2,j} = (\boldsymbol{L}_{2,j}, R_{2,j})$.

3. Radar-Based Imaging Analysis

3.1 SA-Based Method

A number of literature has demonstrated that the SA process enables us for automatically focusing, assuming wider beam imaging scenario. The SA process is also well-known as synthetic aperture radar (SAR) in radio wave band, and provide many promising applications, e.g. terrain-face measurement or subsurface imaging as ground penetrating radar (GPR). In millimeter or sub-millimeter band, the above SA based radar imaging techniques have been developed in recently. Given that the SA process is based on coherent integration, however, the unintended responses due to grating- or side-lobe effects makes it difficult to recognize the shape of the target. Thus, to avoid these above effects, the SA method requires dense data sampling at an interval of less than half of the wavelength in the dielectric medium. In addition, the SA-based method is particularly inaccurate for shape determination of targets having continuous boundaries (*i.e.*, boundaries that cannot be expressed as aggregations of discrete point targets,) because the SA-based method is based on the assumption that the scattering center does not move according to the observation point while, it moves in the case of a continuous boundary. Furthermore, the spectroscopic extended SA mostly requires the band pass filter (BPF) process, so that the dominant frequency in scattering is associated, but it incurs considerably lower range resolution. In addition, in the SA-based method, since each reflection signal with different frequency dependent response would be integrated, the SA image could not directly associate the frequency dependency with each scattering center.

3.2 Spectroscopic RPM Method

3.2.1 RPM Method

The RPM method has been developed as a promising solution to the above problem. Previous studies have demonstrated its effectiveness in imaging scenarios with microwaves and millimeter-range waves [7], [10]. In the RPM method, the range point, $\boldsymbol{q}_{2,i}$, is converted to a scattering center, $\hat{\boldsymbol{p}}(\boldsymbol{q}_{2,i})$ using the following optimization:

$$\hat{\boldsymbol{p}}(\boldsymbol{q}_{2,i}) = \underset{\boldsymbol{p}^{\mathrm{int}}(\boldsymbol{q}_{2,i},\boldsymbol{q}_{2,l},\boldsymbol{q}_{2,m})}{\arg\max} \sum_{j,k} g(\boldsymbol{q}_{2,i}; \boldsymbol{q}_{2,j}, \boldsymbol{q}_{2,k}) \times \exp\left\{-\frac{\|\boldsymbol{p}^{\mathrm{int}}(\boldsymbol{q}_{2,i}; \boldsymbol{q}_{2,j}, \boldsymbol{q}_{2,k}) - \boldsymbol{p}^{\mathrm{int}}(\boldsymbol{q}_{2,i}; \boldsymbol{q}_{2,l}, \boldsymbol{q}_{2,m})\|^2}{\sigma_r^2}\right\}, \tag{1}$$

where, $\boldsymbol{p}^{\mathrm{int}}(\boldsymbol{q}_{2,i}, \boldsymbol{q}_{2,l}, \boldsymbol{q}_{2,m})$ is the point of intersection of the three curves, formed by the propagation path orbit, which is estimated using the relative permittivity of the background. Here, $g(\boldsymbol{q}_{2,i}; \boldsymbol{q}_{2,j}, \boldsymbol{q}_{2,k})$ is expressed as follows;

$$g(\boldsymbol{q}_{2,i}; \boldsymbol{q}_{2,j}, \boldsymbol{q}_{2,k}) \equiv |s(\boldsymbol{q}_{2,j})| \mathrm{e}^{\left\{-\frac{D_{XY,i,j}^2}{2\sigma_{XY}^2} - \frac{D_{Z,i,j}^2}{2\sigma_Z^2} - \frac{D_{R,i,j}^2}{2\sigma_R^2}\right\}} + |s(\boldsymbol{q}_{2,k})| \mathrm{e}^{\left\{-\frac{D_{XY,i,k}^2}{2\sigma_{XY}^2} - \frac{D_{Z,i,k}^2}{2\sigma_Z^2} - \frac{D_{R,i,k}^2}{2\sigma_R^2}\right\}}, \tag{2}$$

where $D_{XY,i,j} = \sqrt{(X_{2,i} - X_{2,j})^2 + (Y_{2,i} - Y_{2,j})}$, $D_{Z,i,j} = |Z_{2,i} - Z_{2,j}|$, and $D_{R,i,j} = |R_{2,i} - R_{2,j}|$. σ_r, σ_{XY}, σ_Z and σ_R are constants, which are usually determined using the interval of the observation sampling as presented in [7]. Thus, intersection point $\boldsymbol{p}^{\mathrm{int}}(\boldsymbol{q}_{2,i}, \boldsymbol{q}_{2,l}, \boldsymbol{q}_{2,m})$ can be accurately calculated using the envelope-based outer-boundary estimation [12], as presented in [10].

3.2.2 Spectroscopic Extension of the RPM Method

To associate the spectroscopic information with RPM imaging, we exploit a unique feature of RPM wherein the range point, $\boldsymbol{q}_{2,i}$, is solely associated with the corresponding scattering center, $\hat{\boldsymbol{p}}(\boldsymbol{q}_{2,i})$. Thus, the information about the frequency-dependent scattering is also associated with $\hat{\boldsymbol{p}}(\boldsymbol{q}_{2,i})$ by a time-frequency analysis of the received signal, $s(\boldsymbol{L}, R)$ around $\boldsymbol{q}_{2,i}$. Here, the dominant frequency response in scattering $\bar{f}$ is calculated at each range point, $\boldsymbol{q}_{2,i}$ as in:

$$\bar{f}(\boldsymbol{q}_{2,i}) = \arg\max_f \frac{|\tilde{S}(f; \boldsymbol{q}_{2,i})|}{|S_{\mathrm{ref}}(f)|}, \tag{3}$$

where $\tilde{S}(f; \boldsymbol{q}_{2,i})$ and $S_{\mathrm{ref}}(f)$ denote the power density spectrum of each observed signal $s(\boldsymbol{L}, t)$ and the reference signal, that is usually formed by the transmitted waveform, respectively. $\bar{f}_{(\boldsymbol{q}_{2,i})}$ is connected to its scattering center as $\hat{p}(\boldsymbol{q}_{2,i})$, and the RPM image, which is an aggregation of the scattering center points. This is associated with the spectroscopic data. As a notable feature of this method, the range points $\boldsymbol{q}_{2,i}$ (the antenna location associated with the range), the scattering center point $\hat{\boldsymbol{p}}(\boldsymbol{q}_{2,i})$, and frequency dependence of the scattering strength $\bar{f}_{(\boldsymbol{q}_{2,i})}$ are associated together with, which is hardly achieved by the SA-based method. In addition, this method does not require the BPF processing to obtain a spectroscopic image, namely, higher range resolution could be maintained, which is another advantage over the SA-based method.

4. Numerical Test

The numerical test based on the three-dimensional FDTD is described as follows. For simplicity, a small dipole is assumed for the transmitter and receiver at the same location, $\boldsymbol{L}$. The induced current waveform is a Gaussian-modulated pulse with a 2.0 THz center frequency and 2.0 THz effective bandwidth. This induced waveform is linearly excited in the x-axis. The pair of transmitting and receiving antennas is scanned along the plane where $z = 0$, and 17 observation points are sampled at equal intervals in the range of $-400\ \mu\text{m} \leqq x, y \leqq 400\ \mu\text{m}$. We assume that the four buried spherical objects and background are lossy media as shown in Fig. 1. The background medium is assumed to be homogeneous and composed of lossy polyethylene terephthalate (PET), which has a relative permittivity of 3.0 and a conductivity of 1.0 S/m. Noiseless case is assumed here.

Here, to validate the frequency dependence of the scattering, each of the four buried objects was assumed to have a dispersive medium according to the Lorentz model [13] as:

$$\varepsilon_r(f) = \varepsilon_\infty + (\varepsilon_s - \varepsilon_\infty)\frac{{f_p}^2}{{f_p}^2 + jf\delta_p/\pi - f^2}, \tag{4}$$

where f_p is the resonant frequency, and δ_p is the coefficient of damping, $\epsilon_s = 3$, $\epsilon_\infty = 1$, and $\delta_p/(2\pi f_p) = 0.1$ are set. Figure 2 shows the Lorentz-based dispersive model, wherein each object has a different resonant frequency f_p. Figure 3 shows the results of the SA-based imaging using the Gaussian band path filter (BPF) with different center frequencies,

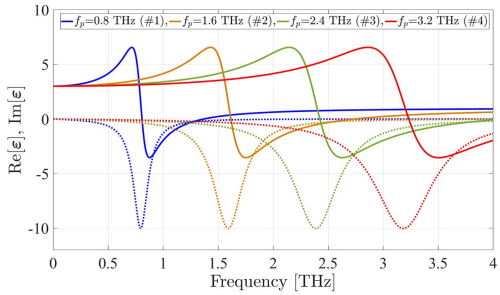

Fig. 2 Frequency characteristic based on Lorentz model for each object (the solid and broken lines represent the real and imaginary parts of the complex relative permittivity, respectively).

for comparison of the methods. The frequency-dependent response can be seen in the SA images, which demonstrates the effectiveness of spectroscopic imaging of the SA-based method. However, their resolutions are considerably limited due to the BPF processing, incurring lower range resolution, and there are some unnecessary responses due to coherent process. Figure 4 shows the results of the proposed method, *i.e.*, the spectroscopic RPM imaging. The results demonstrate that our proposed method provides sufficient spectroscopic quantity to accurately identify the boundary, which is expressed by different colors in Fig. 4. The cumulative error probabilities associated with the proposed method were 41.9% and 100.0%, within the range of $0.1\,\lambda$ ($15\,\mu$m) and $0.2\,\lambda$ ($30\,\mu$m), respectively. The errors are mainly caused by the waveform mismatching between the reference (transmitted) signal and the actual reflection signal from each object, because scattering phenomena on each target boundary is affected by each frequency dependent property of complex permittivity. This errors should be compensated by the waveform estimation scheme, such as in [8].

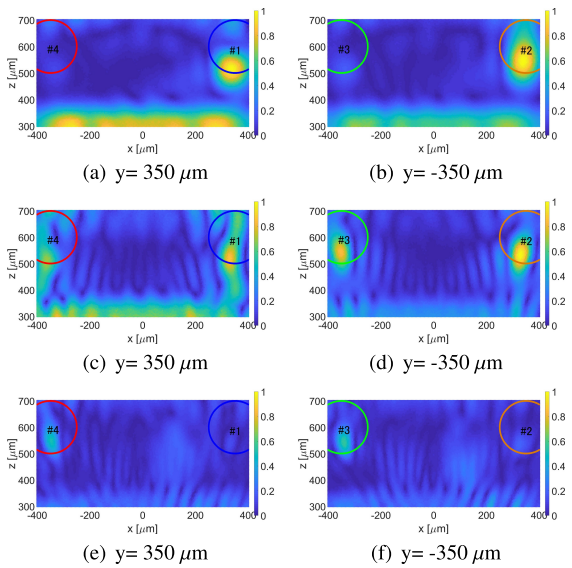

Fig. 3 Cross-sectional images obtained by the SA-based method after applying different BPF. (Red: buried object boundary. Blue: outer medium boundary.) (a), (b): BPF from 1.0 to 2.0 THz, (c), (d): BPF from 2.0 to 3.0 THz, (e), (f): BPF from 3.0 to 4.0 THz.

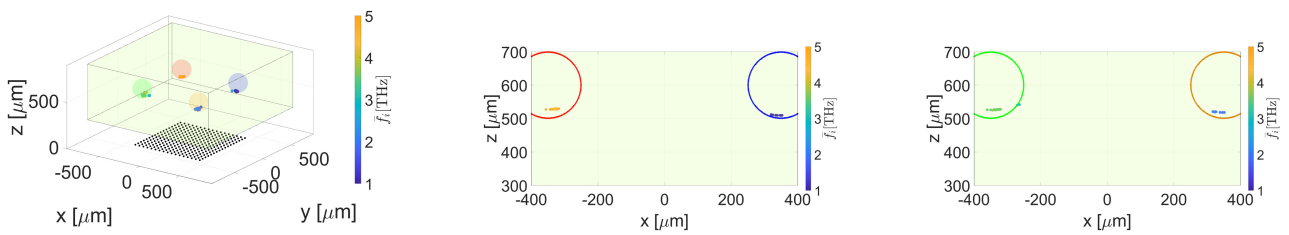

Fig. 4 Spectroscopic image by the RPM method at noiseless scenario. (a) 3-D view, (b) sliced view $330\ \mu\text{m} \leq y \leq 370\ \mu\text{m}$. (c) Sliced view $-370\ \mu\text{m} \leq y \leq -330\ \mu\text{m}$.

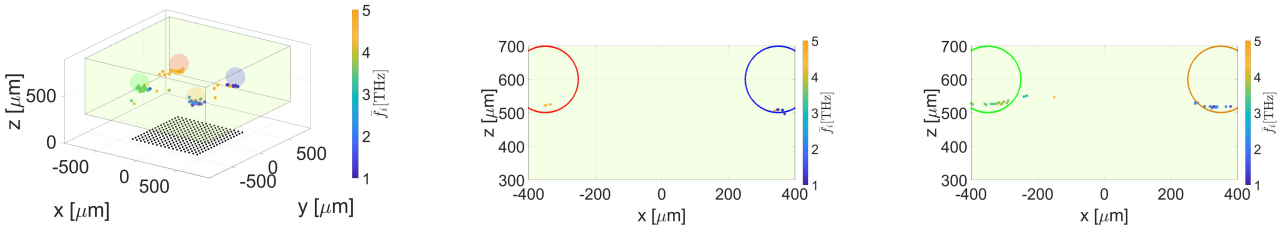

Fig. 5 Spectroscopic image by the RPM method at SNR = 20 dB. (a) 3-D view, (b) sliced view 330 μm $\leq$ y $\leq$ 370 μm. (c) Sliced view -370 μm $\leq$ y ≤ -330 μm.

4.1 Sensitivity to Additive Noise

To assess the noise-robustness of the proposed method, the case, that the received signal includes an additive Gaussian white-noise, is investigated as follows. The signal-to-ratio (SNR) is defined as the ratio of the maximum signal power from buried object (not from surface reflection) to average noise power in the time domain. Figure 5 shows the 3-D imaging results by the proposed method, where the average SNR is approximately 20 dB. The cumulative error probabilities associated with the proposed method were 48.3% and 86.7%, within the range of $0.1\,\lambda$ ($15\,\mu$m) and $0.2\,\lambda$ ($30\,\mu$m), respectively. In the comparison with case noiseless, some scattering center points, obtained by RPM, are deviated from the actual target boundary recognized in Fig. 5, and their spectroscopic response, $\bar{f}_i$, are fluctuated. The reason is that the estimation errors of range points, due to noise, incur the imaging accuracy, and also, the white Gaussian noise could affect the estimation of the dominant frequency of scattering as in Eq. (3). However, these are not severe sensitivity to the additive noise, in both imaging and spectroscopic analysis performance in the proposed method.

5. Conclusion

A novel spectroscopic RPM-based imaging method has been proposed for a wide-beam terahertz imaging scenario. A dispersive FDTD numerical analysis revealed that the proposed method could be used to accurately identify target boundaries based on the spectroscopic features associated with scattering centers. Thus, the spectroscopic feature associated with scattering centers effectively facilitates multi-dimensional imaging and shows promise for future THz imaging applications.

Acknowledgments

This research was supported by JST, PRESTO, Grant Number JPMJPR1771.

References

[1] J. O'Hara and D. Grischkowsky, "Quasi-optic synthetic phased-array terahertz imaging," Journal of the Optical Society of America B—Optical Physics, vol.21, no.6, pp.1178–1191, 2004.

[2] S.C. Henry, L.M. Zurk, S. Schecklman, and D.D. Duncan, "Three-dimensional broadband terahertz synthetic aperture imaging," Optical Engineering, vol.51, no.9, 091603, 2012.

[3] Q. Yang, B. Deng, H. Wang, and Y. Qin, "Experimental research on imaging of precession targets with THz radar," Electron. Lett., vol.52, no.25, pp.2059–2061, Dec. 2016.

[4] Z. Lu, C. Li, X. Gao, and G. Fang, "Study of terahertz LFMCW imaging radar with Hilbert transform receiver," Electron. Lett., vol.50, no.7, pp.549–550, March 2014.

[5] K.B. Cooper, R.J. Dengler, N. Llombart, T. Bryllert, G. Chattopadhyay, E. Schlecht, J. Gill, C. Lee, A. Skalare, I. Mehdi, and P.H. Siegel, "Penetrating 3-D imaging at 4- and 25-m range using a submillimeter-wave radar," IEEE Trans. Microw. Theory Tech., vol.56, no.12, pp.2771–2778, 2008.

[6] K.B. Cooper, R.J. Dengler, N. Llombart, B. Thomas, G. Chattopadhyay, and P.H. Siegel, "THz imaging radar for standoff personnel screening," IEEE Trans. THz Sci. Technol., vol.1, no.1, pp.169–182, Sept. 2011.

[7] S. Kidera, T. Sakamoto, and T. Sato, "Accurate UWB radar three-dimensional imaging algorithm for a complex boundary without range points connections," IEEE Trans. Geosci. Remote Sens., vol.48, no.4, pp.1993–2004, April, 2010.

[8] S. Kidera, T. Sakamoto, and T. Sato, "Super-resolution UWB radar imaging algorithm based on extended capon with reference signal optimization," IEEE Trans. Antennas Propagat., vol.59, no.5, pp.1606–1615, May 2011.

[9] K. Akune, S. Kidera, and T. Kirimoto, "Accurate and nonparametric imaging algorithm for targets buried in dielectric medium for UWB radars," IEICE Trans. Electron., vol.E95-C, no.8, pp.1389–1398, Aug. 2012.

[10] S. Takahashi and S. Kidera, "Acceleration of range points migration-based microwave imaging for nondestructive testing," IEEE Antennas Wireless Propag. Lett., vol.17, no.4, pp.702–705, April 2018.

[11] T. Matsui and S. Kidera, "Spectroscopic range points migration method for wide-beam terahertz imaging" 2018 43rd Int. Conf. on Infrared, Millimeter, and Terahertz Waves (IRMMW-THz), Sept. 2018.

[12] S. Kidera, T. Sakamoto, and T. Sato, "A robust and fast imaging algorithm with an envelope of circles for UWB pulse radars," IEICE Trans. Commun., vol.E90-B, no.7, pp.1801–1809, July 2007.

[13] Z. Li, Z. Zhang, X. Zhao, H. Su, H. Zhang, and J. Lan, "Linewidth extraction from the THz absorption spectra using a modified Lorentz model," Journal of Infrared, Millimeter, and Terahertz Waves, vol.34, no.10, pp.617–626, Oct. 2013.